g-C_3N_4/Bi_2MoO_6 heterojunctions for enhanced visible light photocatalytic oxidation of biomass-derived 5-hydroxymethylfurfural to 2,5-diformylfuran under ambient conditions

Lin-Yu Jiao[a,*], Ze-Long Sun[a], Wen-Yu Luo[a], Ying-Ying Xu[a], Fei Wen[a], Yanfei Xu[b], Zhuo Li[a], Wei Zhao[a], Shanshan Liu[c,*], Mingyue Ding[b,*]

[a] *School of Chemical Engineering, Northwest University, Xi'an, Shaanxi, 710127, P. R. China*
[b] *School of Power and Mechanical Engineering, Wuhan University, Wuhan, Hubei, 430072, P. R. China*
[c] *Shaanxi Key Laboratory of Chemical Additives for Industry, College of Chemistry and Chemical Engineering, Shaanxi University of Science and Technology, Xi'an, Shaanxi, 710021 P. R. China*

E-mail address:
lyjiao@nwu.edu.cn (L.-Y. Jiao),
liushanshan@sust.edu.cn (S. Liu),
dingmy@whu.edu.cn (M. Ding)

Supporting Information

Table of Contents

I. Experimental and Characterization Results

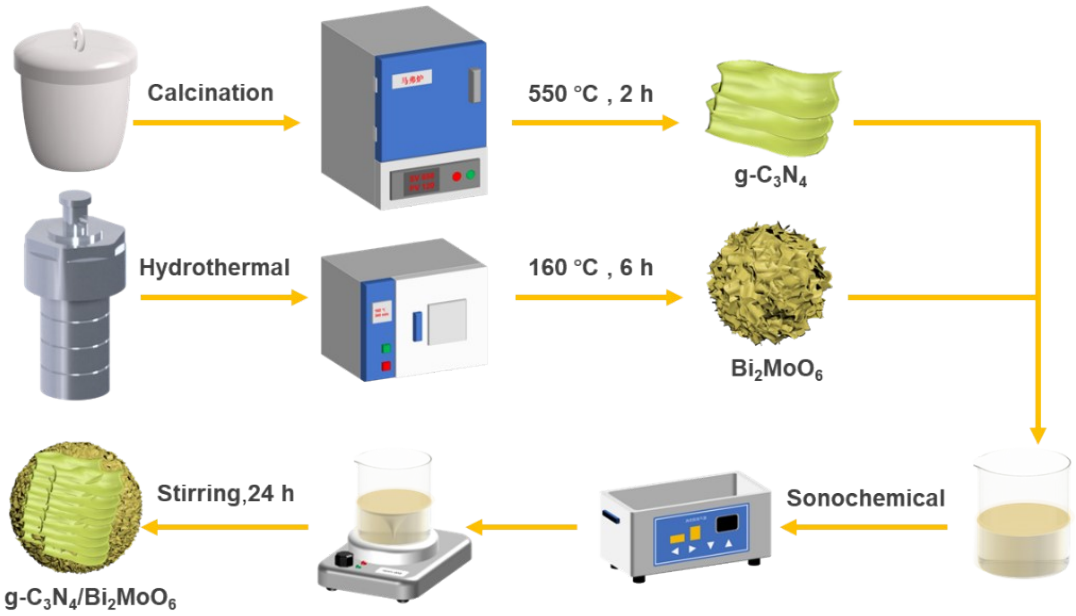

Scheme S1. Illustration of the preparation of CN/BMO composite.

Under aerobic photocatalytic conditions, 5-hydroxymethylfurfural (HMF) underwent selective oxidation to yield 2,5-diformylfuran (DFF) as the product. Reaction mixtures were analyzed using high-performance liquid chromatography (HPLC; Shimadzu LC-20AD system equipped with a C18AQ column, 250 × 4.6 mm, 5 μm). As demonstrated in Figure S1, the chromatographic analysis revealed exclusive detection of HMF and DFF, with no observable byproducts, confirming the high selectivity of the transformation.

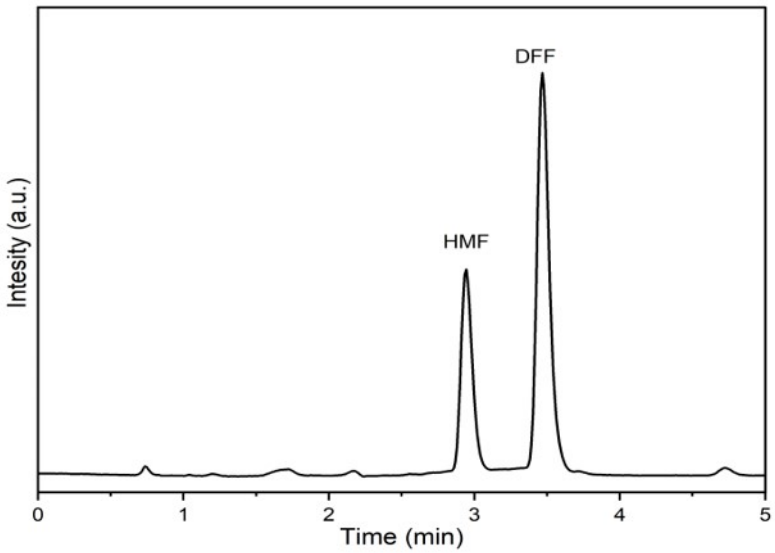

Figure S1. HPLC analysis of HMF and DFF.

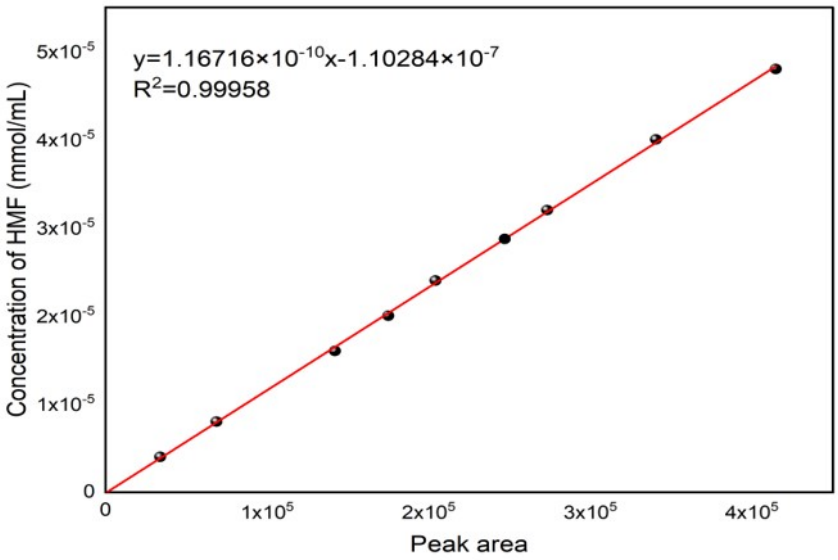

Figure S2. Standard curve of HMF.

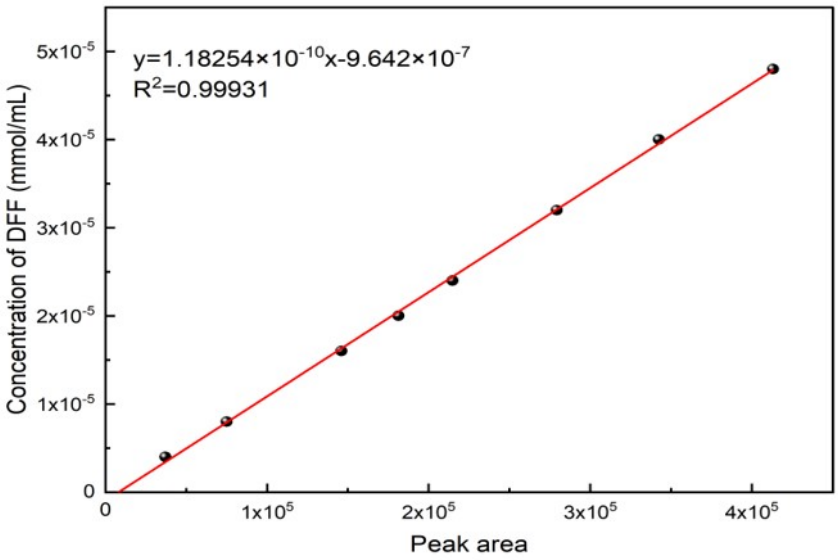

Figure S3. Standard curve of DFF.

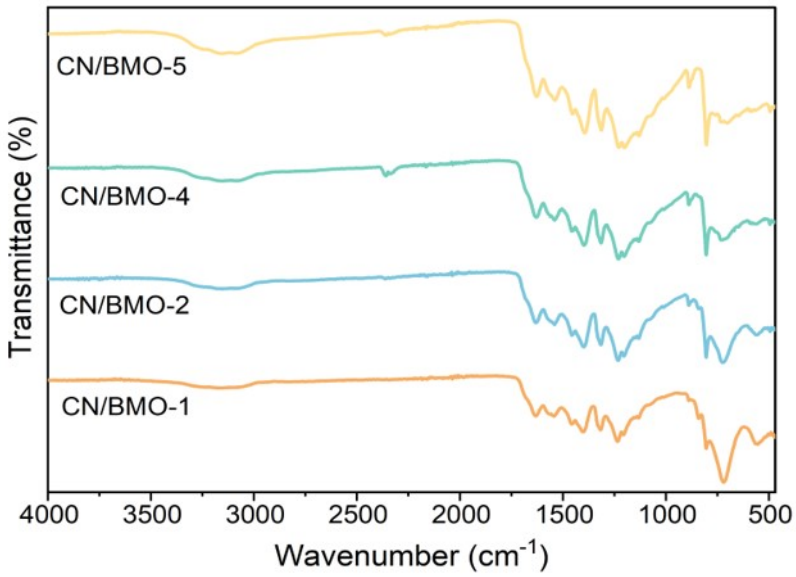

Figure S4. FT-IR spetra of CN/BMO-1, CN/BMO-2, CN/BMO-4, and CN/BMO-5.

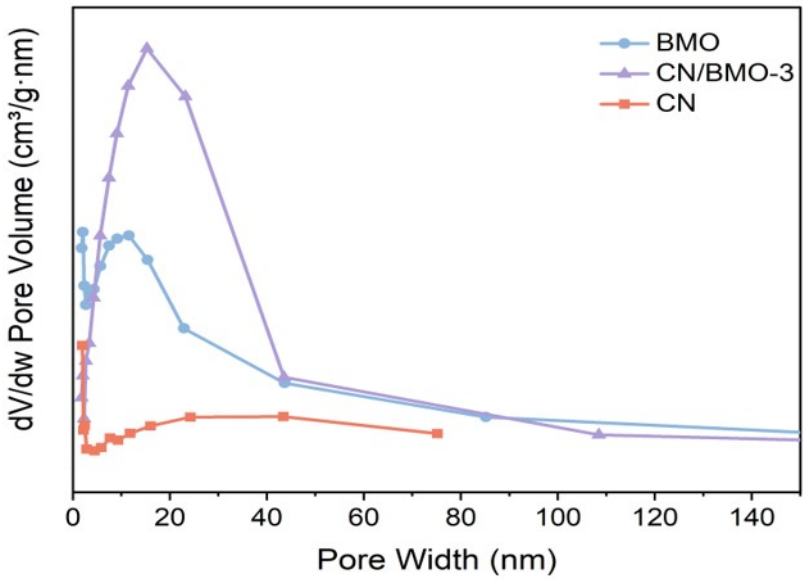

Figure S5. Pore size distribution plots of CN, BMO, and CN/BMO-3.

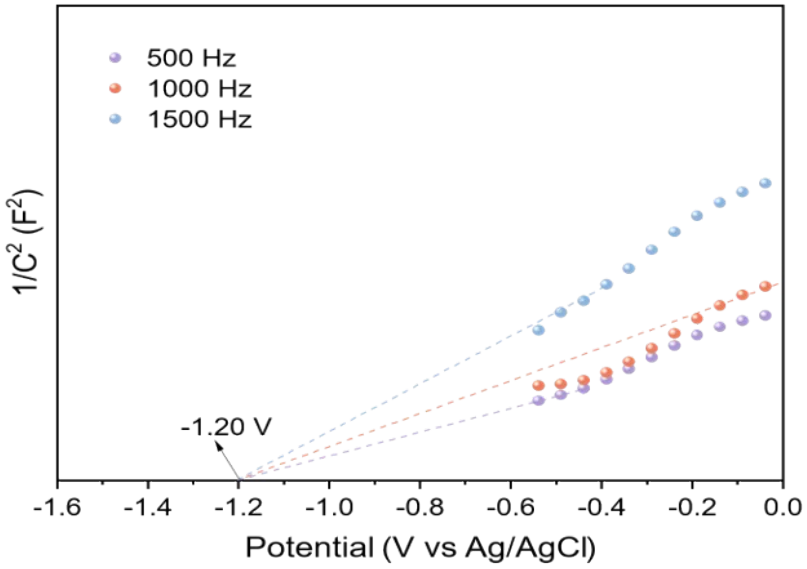

Figure S6. Mott-Schottky curves of CN

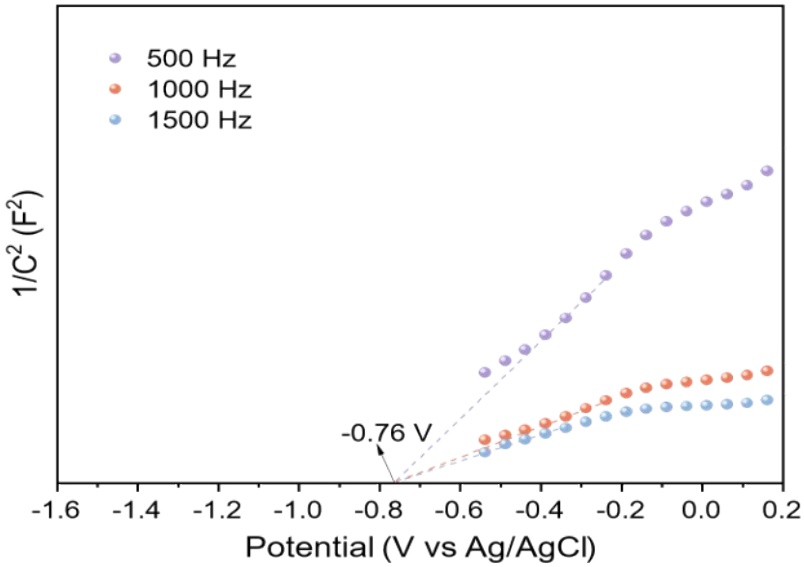

Figure S7. Mott-Schottky curves of BMO.

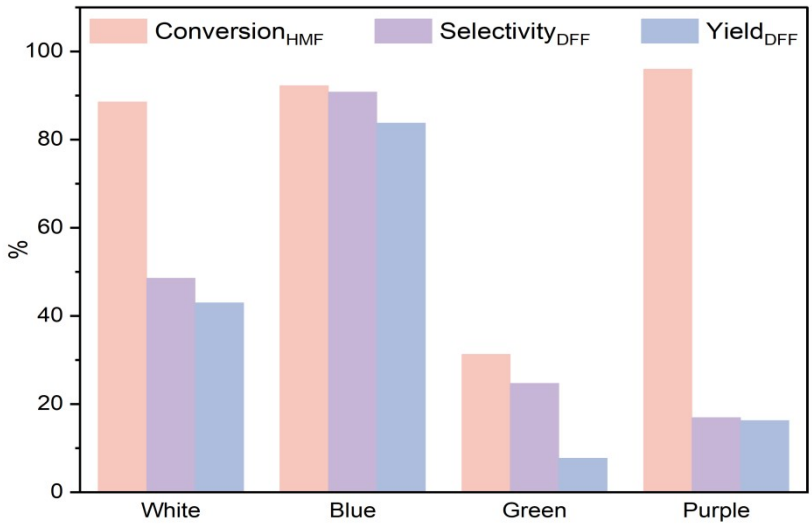

Figure S8. Influence of different wavelengths on photocatalytic oxidation of HMF.

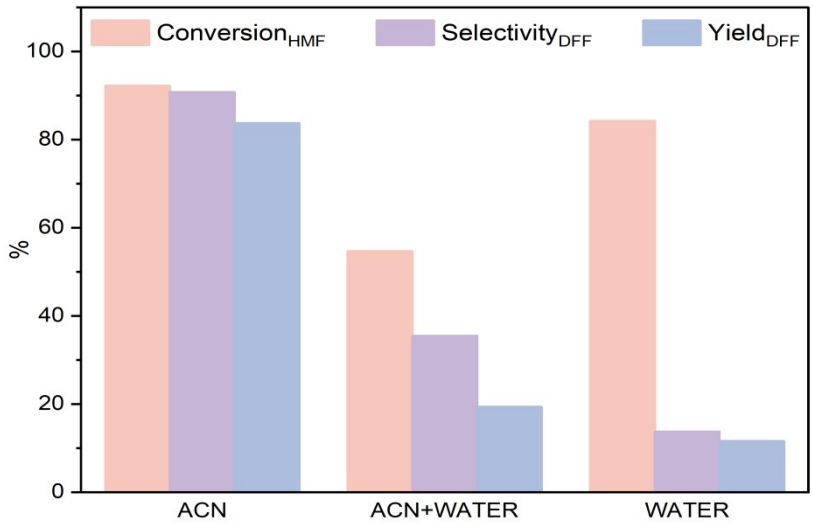

Figure S9. Influence of different solvents on photocatalytic oxidation of HMF.

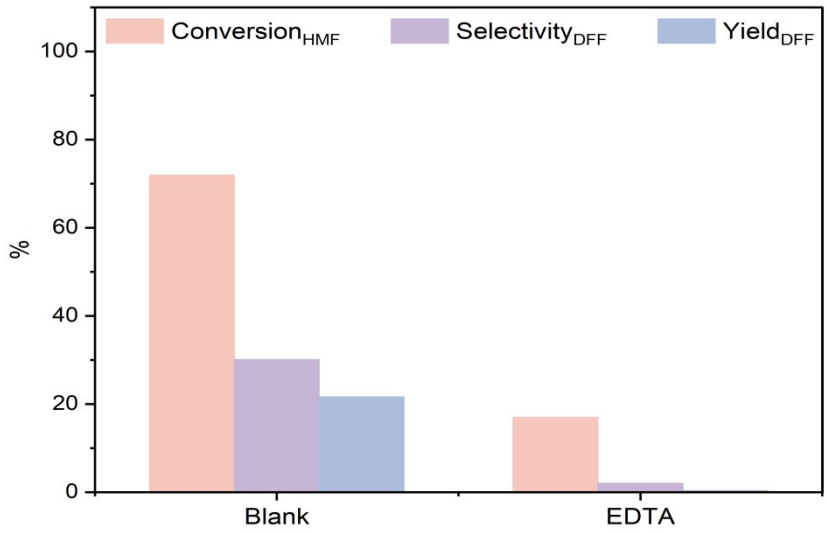

Figure S10. Active species trapping experiments under anaerobic conditions.

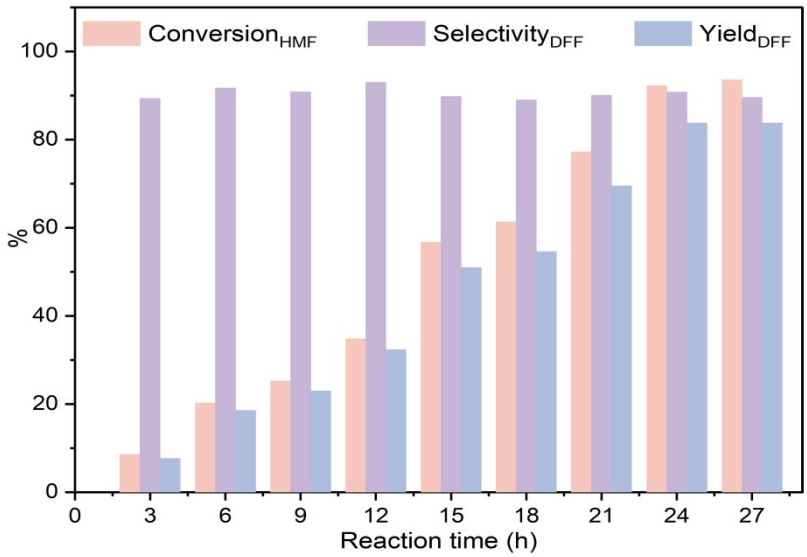

Figure S11. Influence of the reaction time on photocatalytic oxidation of HMF.

The hydrogen peroxide (H_2O_2) production was determined through a standardized iodometric colorimetric method. To 1 mL of the reaction mixture, we sequentially added: 1 mL aqueous KI solution (0.4 M) as the iodide source and 1 mL potassium hydrogen phthalate buffer (0.1 M, pH = 4.0) to maintain optimal acidic conditions. The mixed solution was kept in complete darkness for 2 h to ensure complete reaction while preventing photochemical interference. During this period, H_2O_2 quantitatively oxidizes iodide to form the triiodide anion (I_3^-) according to the following stoichiometric equation:

$$H_2O_2 + 3I^- + 2H^+ \rightarrow I_3^- + 2H_2O$$

The resulting I_3^- complex exhibits a characteristic absorption band at 350 nm, final validation of H_2O_2 generation was performed using diffuse reflectance UV-Vis spectroscopy (DRS).

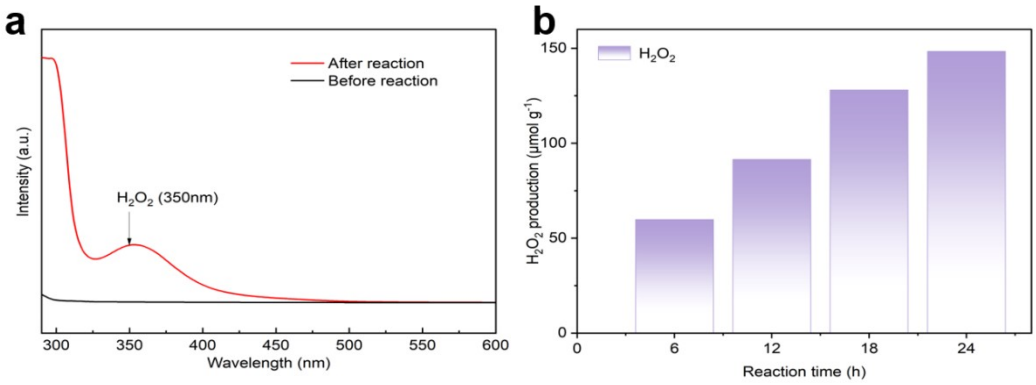

Figure S12. (a) UV–Vis spectra of H_2O_2 production. (b) The H_2O_2 production at different times.

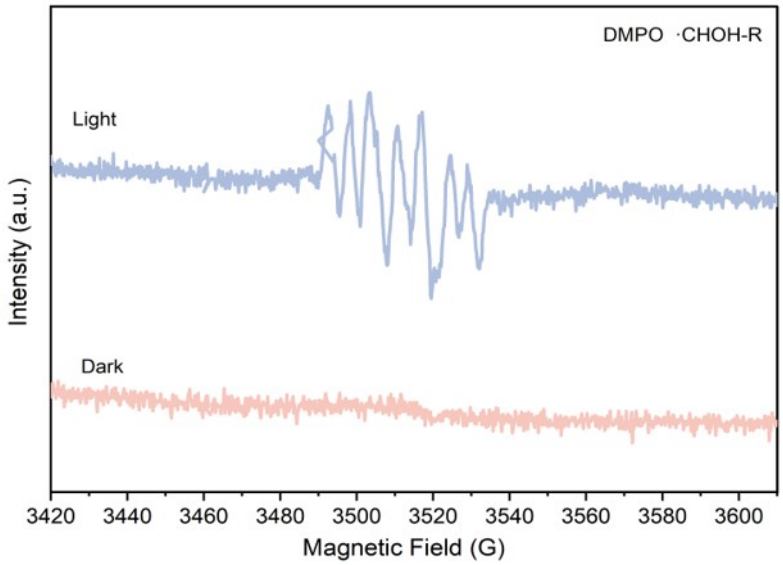

Figure S13. In EPR spectra of CN/BMO-3 were recorded in HMF-containing solution using DMPO as the spin-trapping agent, comparing dark conditions with visible light irradiation.

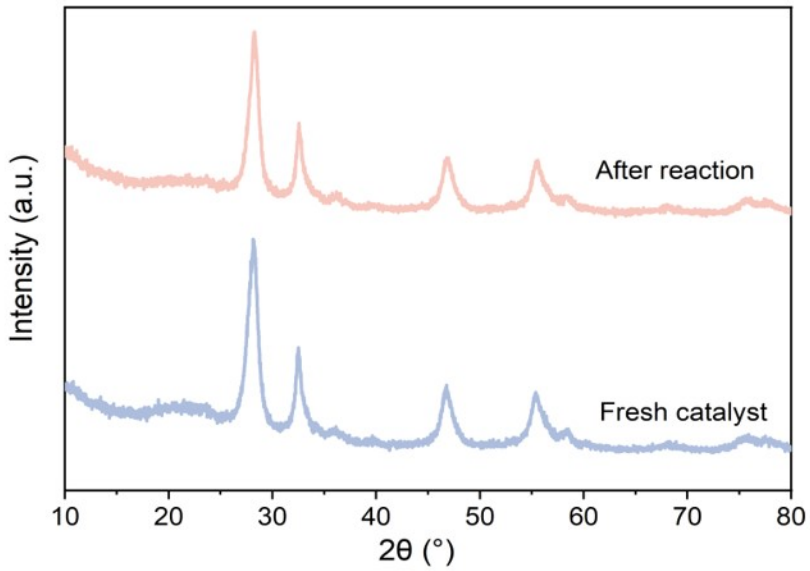

Figure S14. XRD diffraction patterns of CN/BMO-3 before and after the cyclic reaction.

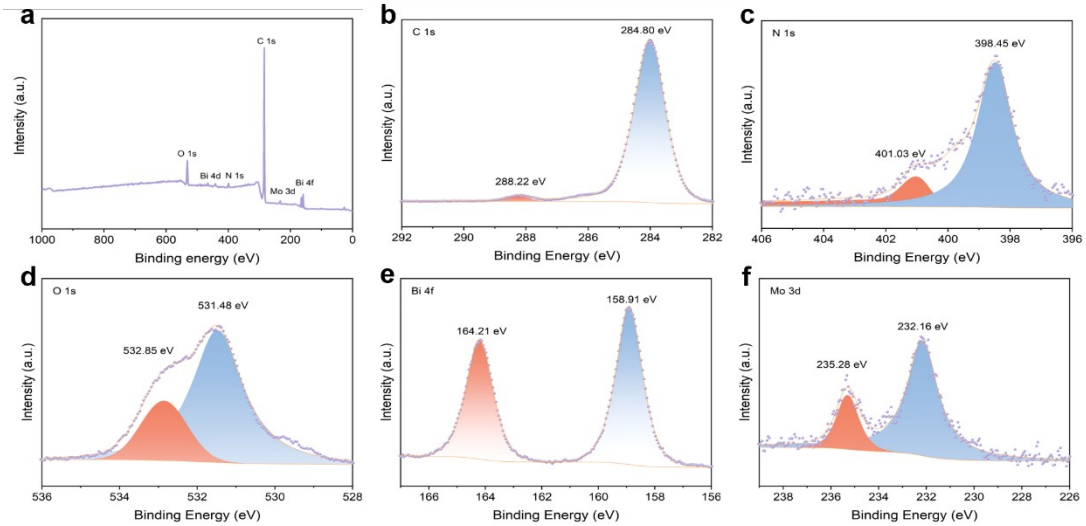

Figure S15. The high resolution XPS spectra of (a) survey spectra, (b) C 1s, (c) N 1s, (d) O 1s, (e) Bi 4f and (f) Mo 3d of CN/BMO-3 after the cyclic reaction.

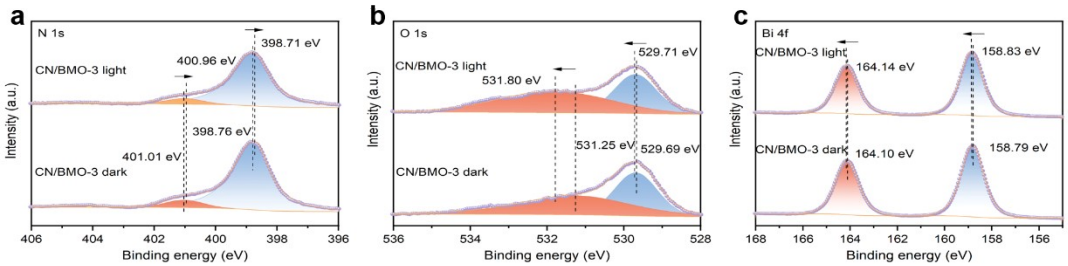

Figure S16. The high resolution XPS spectra of (a) N 1s, (b) O 1s, and (c) Bi 4f of CN/BMO-3 in the dark and light, respectively.

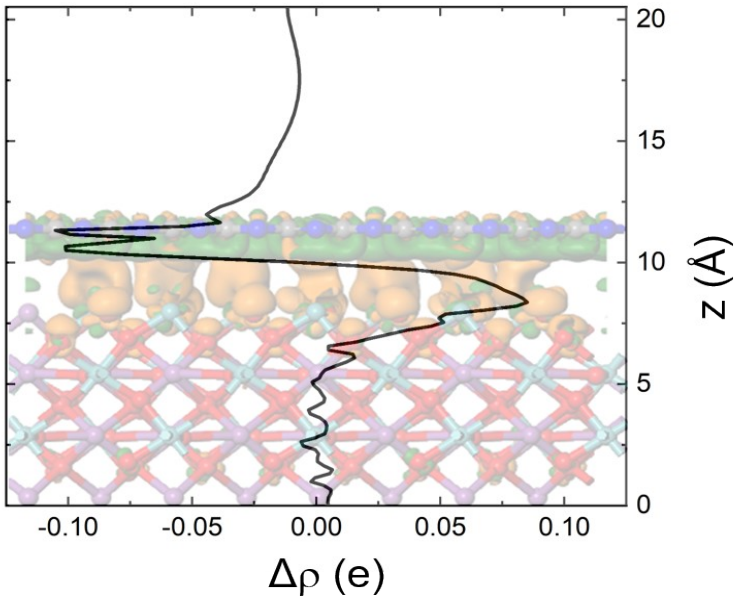

Figure S17. Charge density difference of CN/BMO (***Orange***: electronic accumulation; ***Green***: electronic depletion).

Table S1. Conversion of HMF to DFF using CN/BMO-3 catalyst under varied conditions.

Entry	Catalyst	Light	Atmosphere	Conv. (%)	Select. (%)	Yield. (%)
1	CN/BMO-3	No	Air	trace	-	-
2	No	10 W 455 nm	Air	24.1	-	-
3	CN/BMO-3	10 W 455 nm	N_2	71.9	30.0	21.6
4	CN/BMO-3	10 W 455 nm	Air	92.2	90.8	83.7
5[a]	CN-BMO	10 W 455 nm	Air	67.3	78.2	52.7

[a] Physical mixing of CN and BMO. Reaction conditions: 10 mM of HMF, 40 mg of catalyst, 25 °C, 24 h.

Table S2. Specific surface area, pore volume, and pore size of CN, BMO, and CN/BMO-3.

Catalyst	Specific surface area (m^2/g)	Pore volume (cm^3/g)	Pore diameter (nm)
CN	7.45	0.06	22.43
BMO	32.33	0.16	16.59
CN/BMO-3	44.11	0.22	16.87

II. Comparison of Reaction Results in Recent Studies

Table S3. Comparative of photocatalytic HMF-to-DFF conversion in recent studies.

Catalyst	Reaction conditions	HMF (mM)	Solvent	Conv. (%)	Select. (%)	Yield. (%)	Refs
g-C_3N_4/Bi_2MoO_6	10 W blue LED (λ = 455 nm), Air, 25 °C	10	ACN	92.2	90.8	83.7	This work
UCNT	300 W Xe lamp, Vacuum, 15 °C	10	Water	48.0	95.0	45.6	1
MCN	Fluorescent lamp (340–420 nm), O_2, 25 °C	0.5	Water	50.0	35.0	17.5	2
Fe(III)/ Bi_2MoO_6	500 W Xe lamp, O_2	20	Water	32.6	95.3	31.0	3
Bi_2MoO_6	300 W Xe lamp, O_2, 25 °C	30	ACN	19.0	99.0	18.8	4
NiS_2/CdS	300 W Xe lamp, N_2	10	Water	54.5	95.2	51.9	5
Ni/CdS	8 W blue LED (λ = 440–460 nm), N_2	5	Water	24.6	100	24.6	6
CN-WO_3@MnO_2	10 W blue LED (λ = 420 nm), O_2	0.5	ACN	77.6	79.6	61.8	7
S-vacancy $ZnIn_2S_4$	20 W blue LED (λ = 445 ± 10 nm), Air	5	ACN	96.5	79.9	77.1	8

(1) Our photocatalytic system employs a low-wattage LED lamp (10 W) instead of conventional high-power xenon lamps (typically 300–500 W), demonstrating significant energy efficiency advantages while maintaining high catalytic performance.

(2) In contrast to aerobic oxidation systems requiring continuous O_2 flow, our catalyst achieves complete conversion using only ambient air, representing a greener approach.

(3) While most high-selectivity catalysts utilized sulfides (which suffer from photo- corrosion-induced deactivation), our system employs carbon nitride and bismuth molybdate - non-toxic materials with facile preparation.

(4) The ultrasonication-assisted exfoliation during preparation increases the catalyst's specific surface area and pore volume, thereby providing abundant active sites.

(5) The constructed heterojunction significantly enhances the separation efficiency of photogenerated electron-hole pairs and prolongs charge carrier lifetime, consequently improving photocatalytic activity.

III. References

1. X. Bao, M. Liu, Z. Wang, D. Dai, P. Wang, H. Cheng, Y. Liu, Z. Zheng, Y. Dai and B. Huang, *ACS Catal.*, 2022, **12**, 1919-1929.
2. I. Krivtsov, E. I. García-López, G. Marcì, L. Palmisano, Z. Amghouz, J. R. García, S. Ordóñez and E. Díaz, *Appl. Catal., B*, 2017, **204**, 430-439.
3. J. Xue, C. Huang, Y. Zong, J. Gu, M. Wang and S. Ma, *Appl Organomet Chem*, 2019, **33,** e5187.
4. A. Kumar and R. Srivastava, *ACS Appl. Nano Mater.*, 2021, **4**, 9080-9093.
5. S. Liu, B. Zhang, Z. Yang, Z. Xue and T. Mu, *Green Chem.*, 2023, **25**, 2620-2628.
6. G. Han, Y.-H. Jin, R. A. Burgess, N. E. Dickenson, X.-M. Cao and Y. Sun, *J. Am. Chem. Soc.*, 2017, **139**, 15584-15587.
7. H. Qian, Q. Hou, W. Zhang, Y. Nie, R. Lai, H. Ren, G. Yu, X. Bai, H. Wang and M. Ju, *Appl. Catal., B*, 2022, **319,** 121907.
8. Y. Liu, W. Xue, A. Chowdhury, A. Putta Rangappa and J. Zhao, *Chem. Eng. J.,* 2024, **497,** 154613.